Ultrafast control of electronic states by a terahertz electric field pulse in the quasi-one-dimensional organic ferroelectric $(TMTTF)_2PF_6$

K. Asada,[1] T. Miyamoto,[1,*] H. Yamakawa,[1] J. Hirata,[1] N. Takamura,[1] T. Morimoto,[1] K. Suzuki,[2] T. Otaki,[1] N. Kida,[1] T. Nakamura,[3] and H. Okamoto[1,†]

[1]*Department of Advanced Materials Science, University of Tokyo, Kashiwa 5-1-5, Chiba 277–8561, Japan*

[2]*Department of Applied Physics, University of Tokyo, Bunkyo-ku 113–8656, Japan*

[3]*Institute for Molecular Science, Myodaiji, Okazaki 444–8585, Japan*

(Received 26 June 2021; revised 29 September 2021; accepted 8 November 2021; published 29 November 2021)

A strong terahertz pulse is effective for controlling the macroscopic polarization in ferroelectrics. In the present study, we investigated the response of an organic molecular compound, namely $(TMTTF)_2PF_6$ (TMTTF: tetramethyltetrathiafulvalene), to a strong electric field using terahertz pulse-pump optical-reflectivity probe spectroscopy. This compound undergoes a transition from Mott insulator to charge-order insulator with lowering temperature, and exhibits electronic ferroelectricity in the charge-order phase. When the terahertz pulse is applied in the Mott-insulator phase, an ultrafast reflectivity change proportional to the square of the electric field waveform of the terahertz pulse emerges, which is attributed to the generation of charge disproportionation in each dimer and the resultant creation of macroscopic polarization. When the terahertz pulse is applied in the charge-order phase, an ultrafast reflectivity change proportional to the electric field waveform of the terahertz pulse is observed, which originates from the modulation of the original charge disproportionation and polarization. These ultrafast reflectivity changes can be ascribed to purely electronic responses. In the midinfrared region, where totally symmetric (a_g) modes of intramolecular vibrations coupled with intermolecular charge transfers exist, a large reflectivity change is commonly observed in the Mott-insulator and charge-order phases. To interpret this feature, we constructed a model that incorporates a charge-transfer transition and a_g-mode intramolecular vibrations. The analyses of the results with this model revealed that the change in the reflectivity spectrum by the terahertz electric field can be explained by the energy shift of the charge-transfer transition caused by the electric field-induced change of charge disproportionation in each dimer, and the transfer of the spectral weight from the intradimer charge-transfer (CT) transition to the interdimer CT transition resulting from the weakening of the dimerization. Our model can be used to analyze the optical responses to electric fields in various organic molecular compounds with electron-intramolecular vibration couplings.

DOI: 10.1103/PhysRevB.104.195148

I. INTRODUCTION

Recent developments in femtosecond laser technology have enabled the generation of a nearly monocyclic strong terahertz pulse with an amplitude greater than 100 kV/cm [1,2]. Such a terahertz pulse can be used not only to generate elementary excitations in solids, such as phonons [3], magnons [4,5], and excitons [6–8], but also to control the electronic phase [9,10]. To achieve electronic phase control of a solid through an electric field component of a terahertz pulse, dielectrics are good candidates [11–14]. In particular, in electronic ferroelectrics, whose macroscopic polarizations are created not by displacement of ions but by electron distribution changes, it is expected that rapid control of the polarizations by a terahertz pulse is possible via electric field-induced electron transfers or deformations of electron wave functions [11,15–19]. Most of the electronic ferroelectrics explored to date are organic molecular compounds [20,21]. In fact, in organic molecular ferroelectrics such as TTF-CA (TTF: tetrathiafulvalene and CA: *p*-chloranil) and α-$(ET)_2I_3$ (ET: bis(ethylenedithio)tetrathiafulvalene), polarization control through a terahertz pulse was achieved [11,15–19].

TTF-CA shows a neutral-to-ionic phase transition at $T_c = 81$ K [22–24]. In the ionic phase, ferroelectric polarization is produced via intermolecular charge transfers occurring at the neutral-to-ionic phase transition [21,25,26]. When this compound is irradiated with a terahertz pulse in the ionic phase, the ferroelectric polarization is rapidly modulated along the terahertz electric field waveform through partial charge transfers between the TTF and CA molecules [11]. When this compound is irradiated with a terahertz pulse in the neutral phase with inversion symmetry, thermally excited microscopic ionic domains show large responses to the terahertz electric field, in which characteristic electron and lattice dynamics associated with neutral-ionic domain walls are observed [16].

Concerning α-$(ET)_2I_3$, it has a quarter-filled two-dimensional electronic state and exhibits a metal-to-polar charge-order (CO) transition at $T_c = 135$ K [20,27]. When this compound is irradiated with a terahertz pulse in the polar CO phase, the macroscopic polarization is also modulated along the terahertz electric field through intermolecular partial charge transfers. This electronic response is followed by

*miyamoto@k.u-tokyo.ac.jp
†okamotoh@k.u-tokyo.ac.jp

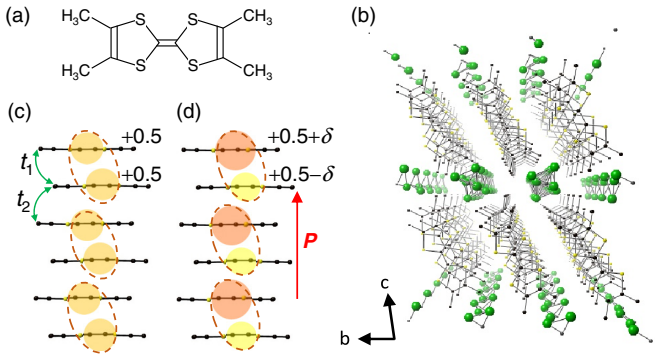

FIG. 1. (a) Molecular structure of TMTTF. (b) Crystal structure of $(TMTTF)_2PF_6$. (c), (d) One-dimensional molecular stacks in (c) the Mott-insulator phase ($T > T_{CO}$) and (d) the CO phase ($T < T_{CO}$). Molecular charges are schematically shown by the colored circles. In the CO phase, a macroscopic polarization P is created by the charge disproportionation.

the subsequent response of the lattice sector or molecular displacements, as evidenced by several types of coherent oscillations on the reflectivity changes in the picosecond time domain [15]. These responses in α-$(ET)_2I_3$ were interpreted according to the fact that the coupling of electron and lattice degrees-of-freedom was significant, and the polar CO was stabilized by molecular displacement. In the metallic phase of α-$(ET)_2I_3$, no prominent responses to a terahertz pulse have been reported. Thus, the dynamical aspects of the responses to a terahertz electric field pulse strongly depend on the electronic states of materials; therefore, more systematic studies on electronic ferroelectrics of organic molecular compounds are desirable. These studies might unravel new aspects of the terahertz electric field-induced responses in electronic ferroelectrics. Considering this background, in the present study we investigated the responses to a terahertz electric field pulse in a quasi-one-dimensional organic molecular compound, namely $(TMTTF)_2PF_6$ (TMTTF: tetramethyltetrathiafulvalene) [28,29].

$(TMTTF)_2XF_6$ (X = P, As, Sb, and Ta) consists of 1D molecular stacks of planar TMTTF molecules [Fig. 1(a)]. The crystal structure of $(TMTTF)_2PF_6$ is shown in Fig. 1(b) [30,31]. One hole exists per two TMTTF molecules, and a quarter-filled quasi-1D electronic state is formed. TMTTF molecules are weakly dimerized as shown in Figs. 1(c) and 1(d). This dimerization is due to the presence of anions XF_6. By lowering the temperature and applying the pressure, this series of compounds shows a variety of electronic phases [32–36] because of strong Coulomb interactions between electrons and electron-lattice interactions [37–39]. $(TMTTF)_2PF_6$ studied here shows four different phases: a metal phase, a Mott-insulator phase, a polar CO phase, and a spin-Peierls phase. By lowering the temperature from room temperature, the resistivity decreases, reaching a minimum at approximately 250 K ($=T_\rho$) [29,40]. Below this temperature, the resistivity increases with decreasing temperature, showing semiconducting behavior, and this compound enters the Mott-insulator phase. With a further decrease in temperature, the compound undergoes a transition from a Mott-insulator phase to a CO phase at $T_{CO} = 67$ K [41], and then enters the spin-Peierls phase at 19 K [31,42]. The charge distributions in the Mott-insulator and CO phases are schematically shown in Figs. 1(c) and 1(d), respectively. Ovals represented by broken lines indicate dimers. In the Mott-insulator phase, the charge of each molecule is +0.5, and the two molecules in each dimer are crystallographically equivalent. By contrast, in the CO phase, the charges of the two molecules are disproportionate as $\rho = 0.5 + \delta$ and $\rho = 0.5 - \delta$ owing to the intermolecular electron correlations [37–39], while structural parameters hardly change [43]. The magnitude of charge disproportionation, i.e., 2δ, was evaluated to be 0.28 in the NMR experiments [42] and 0.10–0.15 in the infrared (IR)- and Raman spectroscopy in $(TMTTF)_2PF_6$ [29]. In addition, it is considered that the inversion symmetry is lost and the system is in a polar or ferroelectric state, although macroscopic polarization has not been measured because of the low resistivity even at low temperatures. Below $T_{SP} = 19$ K, this compound enters the spin-Peierls phase, in which tetramerization occurs and the spin susceptibility decreases [42], although the CO pattern remains essentially unchanged [31]. Detailed x-ray structural analyses revealed that the molecular displacements during tetramerization at 19 K are on the order of 0.01 Å [31]. This suggests that the change in the electronic state across this transition would be negligibly small.

To investigate the responses to terahertz electric fields in both the Mott-insulator phase and CO phase, we used a terahertz-pump optical-reflectivity probe spectroscopy. In organic molecular compounds, intramolecular vibrations sometimes play important roles in physical properties [44–48]. It was reported that in $(TMTTF)_2PF_6$ the optical reflectivity and conductivity spectra in the mid-IR region show anomalous structures [29,32], and they originate from the strong coupling between the electron degree of freedom and intramolecular vibrations. If a terahertz-field-induced change is detected in the spectrum associated with intramolecular vibrations as well as that associated with intermolecular electronic transitions, important information can be deduced about the coupling of those vibrations to the electronic state in both the Mott-insulator and the polar CO phases.

The remainder of this paper is organized as follows. In Sec. II, we describe the details of the conducted experiments. In Sec. III, we present and discuss the experimental results. In Sec. III A, we report the imaging of polar CO domains. In Secs. III B and III C, we show the steady-state optical spectra and their analyses, respectively. Based on the results of these subsections, we report the changes in reflectivity and optical conductivity spectra caused by the terahertz pulse. The electric field-induced changes in the electronic and vibronic states are discussed in Secs. III D–III H. In Sec. IV, we summarize our study.

II. EXPERIMENT DETAILS

A. Sample preparations

Single crystals of $(TMTTF)_2PF_6$ were grown by an electrochemical oxidation method previously reported [49]. The typical size of the crystal is 2 mm along the a axis and 0.4 mm along the b' axis. Here, the b' axis is in the ab plane and perpendicular to the a axis. The typical thickness of the crystal is 0.2 mm.

B. Terahertz radiation imaging

For terahertz radiation imaging of ferroelectric domains, a femtosecond laser pulse delivered from a mode-locked Ti: sapphire laser with a central wavelength (photon energy) of 800 nm (1.55 eV), a repetition rate of 80 MHz, and a pulse width of approximately 100 fs, was focused on the *ab'* plane of a single crystal. The spot diameter d of the crystal surface of the incident femtosecond laser pulse was approximately 30 μm, which was the spatial resolution in this experiment. The electric field E of the laser pulse was parallel to the a axis ($E \| a$). The electric field waveform $E_{\mathrm{THz}}(t)$ of the terahertz radiation emitted from the crystal was measured with a low-temperature grown GaAs detector in a transmission configuration. Details of the detection method were reported in Ref. [50]. The phase and amplitude of $E_{\mathrm{THz}}(t)$ depend on the direction and magnitude of the ferroelectric polarization, respectively [50–53]. By using a raster scan, we could map out the amplitudes of the ferroelectric polarization and visualize the ferroelectric-domain structures. The absorption depth of the incident laser pulse polarized along the a axis was approximately 20 μm; this depth was estimated from the absorption spectrum obtained from the polarized reflectivity spectrum using the Kramers-Kronig transformation.

C. Measurements of steady-state and transient reflectivity spectra

The steady-state polarized reflectivity spectrum along the a axis was measured on the ab plane of a single crystal using a Fourier-transform IR spectrometer equipped with a microscope and a specially designed cryostat.

In the terahertz pulse-pump optical-reflectivity probe measurements, a Ti: sapphire regenerative amplifier with a central wavelength (photon energy) of 800 nm (1.55 eV), a repetition rate of 1 kHz, a pulse width of 90 fs, and a pulse energy of 5 mJ was used as the light source. The output of the regenerative amplifier was divided into two beams. One beam was used for the generation of a terahertz pump pulse. A strong terahertz pulse was generated using a pulse-front tilting method for optical rectification in a nonlinear crystal $LiNbO_3$ [1,54]. The electric field waveform of the terahertz pulse was measured through electro-optical (EO) sampling in which a ZnTe crystal with a thickness of 200 μm was used as an EO crystal. The methods of generation and detection of terahertz pulses were comprehensively reported in Ref. [55]. The maximum electric field amplitude of the terahertz pulse was approximately 300 kV/cm in a cryostat. The time origin ($t_{\mathrm{d}} = 0$ ps) was set at the time at which the absolute value of the terahertz electric field reached a maximum.

The other beam from the regenerative amplifier was used as the excitation light of an optical parametric amplifier, from which probe pulses from 0.1 to 0.75 eV with a temporal width of approximately 90 fs were obtained. The delay time t_{d} of the probe pulse relative to the pump pulse was varied by changing the path length of the probe pulse with a mechanical delay stage. The spot diameters of the terahertz pump pulse and the probe pulse were approximately 200 and 100 μm, respectively. The polarizations of the pump and probe pulses were both parallel to the a axis, that is, to the molecular stacking axis.

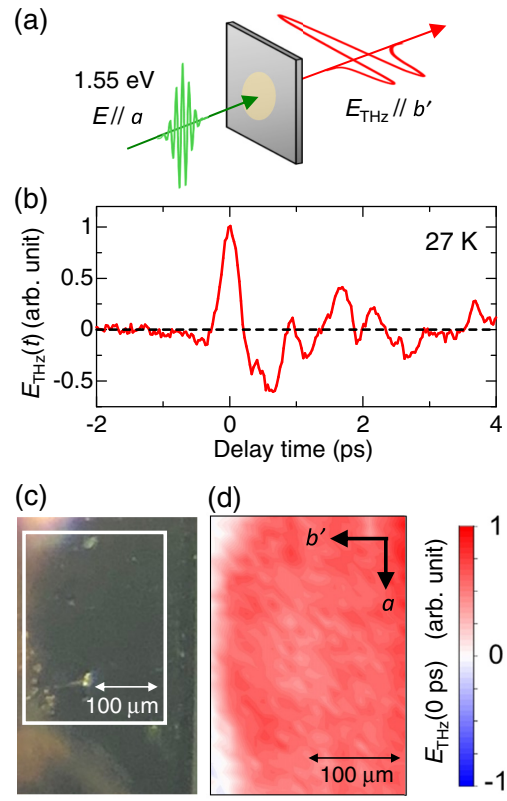

FIG. 2. Terahertz-radiation imaging on $(TMTTF)_2PF_6$. (a) The experimental configuration. (b) A typical electric field waveform, $E_{\mathrm{THz}}(t)$, of the terahertz radiation measured at 27 K. (c) The photograph of the ab' plane of the crystal. (d) The terahertz radiation image on the ab' plane measured at 27 K.

III. RESULTS AND DISCUSSION

A. Terahertz radiation imaging of ferroelectric domains in the CO phase

To characterize the ferroelectric-domain structure in the ferroelectric CO phase, we performed the terahertz radiation imaging in a transmission configuration, as illustrated in Fig. 2(a). In the CO phase, $(TMTTF)_2PF_6$ belongs to point group P1 and does not have spatial inversion symmetry [31]. In this case, it is expected that terahertz waves with an electric field E_{THz} both parallel (||) and perpendicular ($\perp$) to the a axis are generated by the irradiation of a femtosecond laser pulse with an electric field $E \| a$ via optical rectification process, which is a type of second-order nonlinear optical process. The magnitude of the terahertz wave was dominated by the coherence length of the terahertz radiation process, i.e., L_{c}, which is expressed as follows:

$$L_{\mathrm{c}} = \frac{\pi c}{\omega_{\mathrm{THz}} |n_{\mathrm{g}} - n_{\mathrm{THz}}|} . \tag{1}$$

Here, c is the speed of light, ω_{THz} and n_{THz} are the frequency and refractive index of the radiated terahertz wave, respectively, and n_{g} is the group refractive index of the incident laser pulse. When the photon energy of the incident laser pulse ($E \| a$) is 1.55 eV and the frequency of the emitted terahertz wave is assumed to be 1 THz, L_{c} is approximately

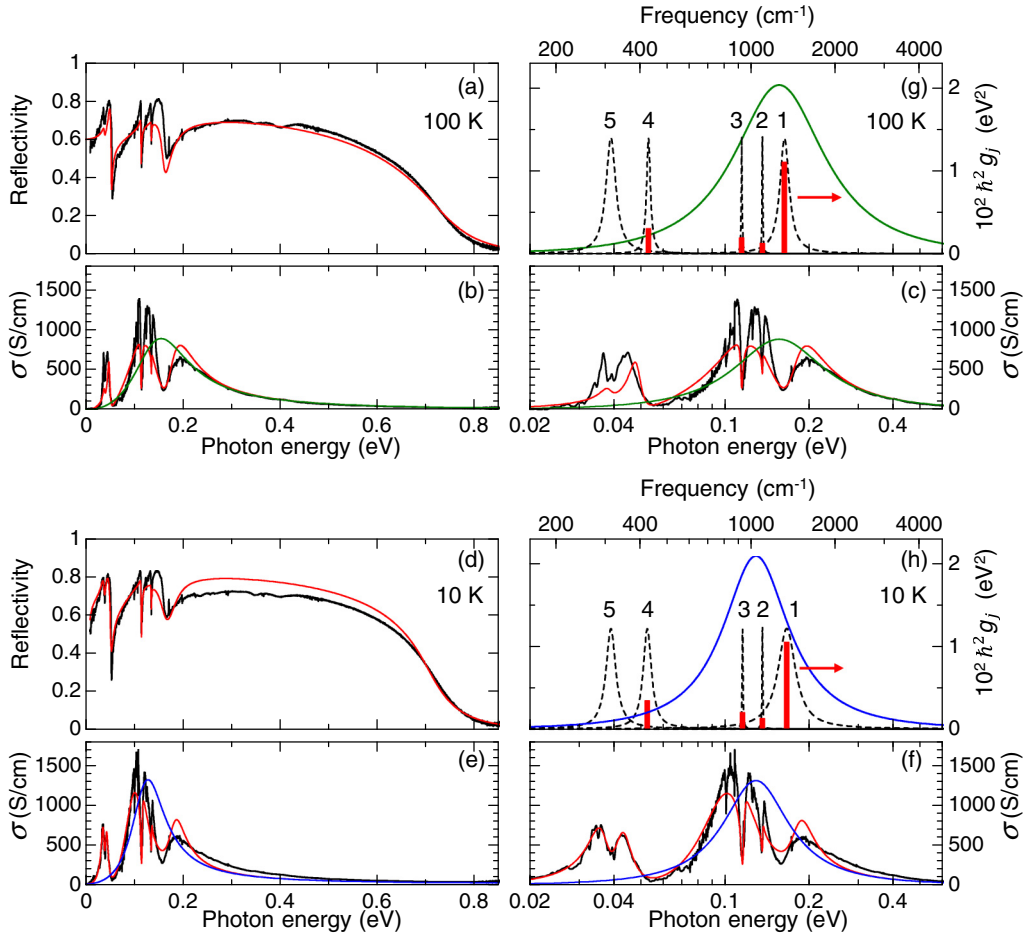

FIG. 3. (a) The polarized reflectivity spectrum measured with $E||a$ at 100 K in $(TMTTF)_2PF_6$. (b), (c) The optical conductivity (σ) spectrum for $E||a$ at 100 K. (d) The polarized reflectivity spectrum measured with $E||a$ at 10 K. (e), (f) The optical conductivity (σ) spectrum for $E||a$ at 10 K. The red lines in (a)–(f) are fitting curves. The green lines in (b), (c) and blue lines (e), (f) are the simulated σ spectrum for the CT transition without EMV couplings. (g), (h) Lorentz oscillators of a_g modes $j = 1-5$ plotted in a normalized scale (broken lines) and the magnitudes of the parameter $\hbar^2 g_j$ (red bars): (g) 100 K and (h) 10 K. The green line in (g) and the blue line in (h) are the simulated σ spectra for the CT transition without EMV couplings shown in an arbitrary unit.

14 μm for $E_{THz}||a$ and 200 μm for $E_{THz} \perp a$, or equivalently $E_{THz}||b'$. For these evaluations, we used the following values of refractive index: $n_{THz} = 12.2$ for $E_{THz}||a$, $n_{THz} = 2.1$ for $E_{THz}||b'$, and $n_g = 1.39$ for $E||a$ at 1.55 eV. These values were simply estimated from the reflectivity values. For the terahertz region, we used a reflectivity value of 0.72 at approximately 55 cm^{-1}, as reported in Ref. [29]. For 1.55 eV, we used the reflectivity value measured in this study. The thickness of the single crystal used in this measurement was 90 μm, which is much longer than L_c for $E_{THz}||a$, so that the terahertz radiation in that configuration should be suppressed. Therefore, in our study, we measured the terahertz radiation for $E_{THz}||b'$. The measurement temperature was 27 K, notably below $T_{CO} = 67$ K.

A typical electric field waveform of the radiated terahertz wave, denoted as $E_{THz}(t)$, is shown in Fig. 2(b). The time at which the electric field amplitude reached a maximum was set as the time origin. The electric field amplitude $E_{THz}(0)$ is proportional to the intensity of the incident femtosecond laser pulse (not shown). Therefore, we can consider that the terahertz wave is radiated via the optical rectification process, and $E_{THz}(0)$ is proportional to the magnitude of the ferroelectric polarization [50–53]. Figure 2(c) shows a photograph of the crystal. We measured $E_{THz}(0)$ in the region surrounded by the white rectangle in Fig. 2(c) and expressed its position dependence using the color distribution in Fig. 2(d). As shown in Fig. 2(d), $E_{THz}(0)$ is almost constant in the measured spatial region (~200 μm × 300 μm), indicating that the crystal consists of a single domain or a large size of ferroelectric domains in the CO phase. The domain size is sufficiently large compared to the spot sizes of the pump and probe pulses, approximately 200 and 100 μm, respectively. We ascertain that no terahertz radiation was observed in the Mott-insulator phase above T_{CO}.

B. Steady-state optical reflectivity and conductivity spectra

Figures 3(a) and 3(d) show polarized reflectivity (R) spectra with $E||a$ at 100 K in the Mott-insulator phase and at 10 K in the CO phase, respectively, for $(TMTTF)_2PF_6$ [56]. No prominent structures are observed in the polarized R spectra with $E \perp a$, or equivalently $E||b'$, except for several sharp structures due to phonons (not shown). The spectra

with $E \| a$ in Figs. 3(a) and 3(d) are roughly consistent with previously reported spectra [32,35]. At both temperatures, a broad high-reflection band is observed below 0.7 eV, which is ascribed to intermolecular transition. This band was sometimes referred to as the charge-transfer (CT) transition band. Below 0.2 eV, complicated sharp structures are superimposed on the broad CT band. These structures are considered to originate from intramolecular vibrations of TMTTF coupled with intermolecular CT via electron-intramolecular vibration (EMV) coupling [32,57]. Both broad CT and sharp structures are commonly observed at 100 and 10 K, while the reflectivity is slightly larger at 10 K in the CO phase than at 100 K in the Mott-insulator phase over the entire range.

Using the Kramers-Kronig transformation, we converted the R spectra to the optical conductivity (σ) spectra, which are shown on a linear scale in Figs. 3(b) and 3(e), and on a log scale in Figs. 3(c) and 3(f). The spectral shapes of σ at 100 and 10 K are similar to each other; broad absorption exists at approximately 0.2 eV, while several sharp structures emerge below 0.15 eV. These structures are attributed to the EMV couplings mentioned above. The σ spectrum at 10 K has a spectral weight on the side presenting slightly lower energy than at 100 K. This difference is ascribed to the changes in the transfer integrals between neighboring molecules with a decrease in temperature. The energy of the CT transition is scaled by the dimerization gap $2(t_1 - t_2)$ [58], where t_1 and t_2 are the intradimer and interdimer transfer integrals, respectively, as indicated in Fig. 1(c). With a decrease in temperature, the difference between t_1 and t_2 decreases, while the average value of t_1 and t_2, i.e., $(t_1 + t_2)/2$, remains almost unchanged [43]. This leads to expect a decrease in the CT transition energy at lower temperatures. The observed low-energy shift of the CT transition energy from 100 to 10 K is consistent with this tendency.

C. Analysis of steady-state optical reflectivity and conductivity spectra

To understand the complicated spectra under the influence of EMV couplings in this type of quarter-filled 1D molecular system, analyses were conducted with the dimer model [32,48,59] and the 1D model, which is more generalized [60]. In the present study, to analyze both the steady-state optical spectra and their electric field-induced changes, we adopted a simple model in which the effects of EMV couplings are introduced as interactions between classical oscillators [56]. Later we will show that this classical model is almost equivalent to the dimer model used in the previous studies.

In our model, we assume that the optical response in $(TMTTF)_2PF_6$ is only caused by the CT transition and intramolecular vibrations. We consider the CT transition as a classical oscillator with a frequency ω_{CT}, damping constant γ_{CT}, and effective charge ρ. We also consider intramolecular vibration j as a classical oscillator with frequency ω_j and damping constant γ_j. In general, totally symmetric (a_g) modes of intramolecular vibrations are strongly coupled with electrons in this type of molecular compound. In our model, therefore, we assume that all of the IR-active phonons observed for $E \| a$ are those a_g modes, and no other IR-active modes exist. In this case, a phonon oscillator (an a_g mode of intramolecular vibration) has no charge. The oscillators of these phonons are coupled with the oscillator of the CT transition, as illustrated in Fig. 4. When an electric field of light is applied to this system, an oscillator of phonons is not driven directly but driven by the coupling with the CT transition, which is the EMV coupling. In the analysis of the σ spectra, we assume five oscillators of phonons (see Fig. 4).

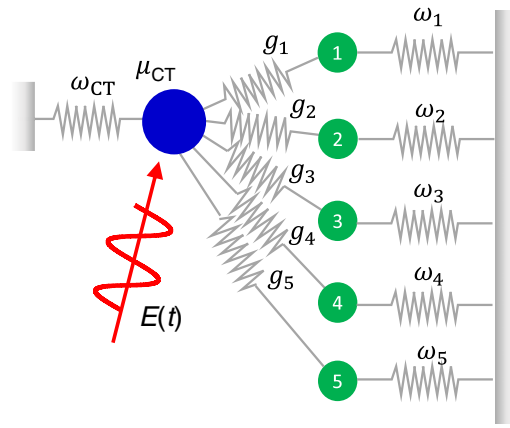

FIG. 4. A schematic of the classical model for analyzing the optical spectra of the system consisting of an electronic (CT) transition and the a_g-mode intramolecular vibrations $j = 1$–5. μ_{CT} is a physical quantity corresponding to the transition dipole moment of the CT transition. ω_{CT} and ω_j are the frequencies of the CT transition and the a_g-mode intramolecular vibration j, respectively. g_j is the parameter dominating the interaction between the CT transition and each a_g mode.

The equation of motions in this system is as follows:

$$\begin{pmatrix} L_{CT}^{-1} & g_1 & g_2 & \cdots & g_5 \\ g_1 & L_1^{-1} & 0 & \cdots & 0 \\ g_2 & 0 & L_2^{-1} & \cdots & 0 \\ \vdots & \vdots & \vdots & \ddots & \vdots \\ g_5 & 0 & 0 & \cdots & L_5^{-1} \end{pmatrix} \begin{pmatrix} x_{CT} \\ x_1 \\ x_2 \\ \vdots \\ x_5 \end{pmatrix} = \begin{pmatrix} C \\ 0 \\ 0 \\ \vdots \\ 0 \end{pmatrix} E(\omega), \tag{2}$$

where L_{CT} and L_j ($j = 1-5$) are Lorentz oscillators of the CT transition and intramolecular vibration j, respectively, which are expressed as follows:

$$L_{CT} = \frac{1}{\omega_{CT}^2 - \omega^2 - i\omega\gamma_{CT}}, \quad L_j = \frac{1}{\omega_j^2 - \omega^2 - i\omega\gamma_j}, \tag{3}$$

where g_j is the coupling constant between the CT transition and intramolecular vibration j, which is proportional to the EMV coupling constant. Equation (2) can be regarded as the classical description of the Fano interference [61–64]. This model is useful because it can be easily extended to a system having a coupling of the electronic transition with an IR-active mode by setting the charge of an IR-inactive oscillator to a finite value.

Expressing the 6×6 matrix on the left side of the equation of motion [Eq. (2)] as $\boldsymbol{M}$, the linear susceptibility $\chi(\omega)$ can be

described using the (1,1) entry of $\boldsymbol{M}^{-1}$:

$$\chi(\omega) = \mu_{\mathrm{CT}}^2 (1 \quad 0 \quad 0 \quad 0 \quad 0 \quad 0) \boldsymbol{M}^{-1} \begin{pmatrix} 1 \\ 0 \\ 0 \\ 0 \\ 0 \\ 0 \end{pmatrix}. \quad (4)$$

Here, μ_{CT} is the magnitude of the transition dipole moment of the CT transition. By using the dielectric constant at high frequencies, ε_∞, the complex dielectric constant $\tilde{\varepsilon}(\omega)$, and real part of the optical conductivity $\sigma(\omega)$ in this system can be obtained from Eq. (4) as follows:

$$\tilde{\varepsilon}(\omega) = \varepsilon_\infty + \frac{\varepsilon_0 {\mu_{\mathrm{CT}}}^2 L_{\mathrm{CT}}}{1 - L_{\mathrm{CT}} \hat{D}_{\mathrm{F}}},$$

$$\hat{D}_{\mathrm{F}} = \sum_{j=1}^{5} g_j^2 L_j, \quad \sigma(\omega) = \mathrm{Im}\left[\frac{\omega \varepsilon_0 {\mu_{\mathrm{CT}}}^2 L_{\mathrm{CT}}}{1 - L_{\mathrm{CT}} \hat{D}_{\mathrm{F}}}\right]. \quad (5)$$

Before applying this model, we show that Eq. (5) can represent a wider range of electronic states than a simple dimer model. According to Eqs. (2.20), (2.21), and (2.23) in Ref. [48], the optical conductivity of the N isolated dimers in the volume Ω, $\sigma_{\mathrm{d}}(\omega)$, is written as

$$\sigma_{\mathrm{d}}(\omega) = \mathrm{Im}\left[\frac{\omega \frac{1}{4} e^2 a^2 \frac{N}{\Omega} \frac{2\omega_{\mathrm{CT}}}{\hbar} |\langle E_+|\delta\hat{n}|E_-\rangle|^2 L_{\mathrm{CT}}(\omega)}{1 - \frac{2\omega_{\mathrm{CT}}}{\hbar^2} |\langle E_+|\delta\hat{n}|E_-\rangle|^2 L_{\mathrm{CT}}(\omega) \sum_j \omega_j \tilde{g}_j^2 L_j(\omega)}\right], \quad (6)$$

where e is the elementary charge, a is the distance between the nearest-neighbor molecules, $|E_-\rangle$ ($|E_+\rangle$) is the ground state (CT-excited state), $\delta\hat{n} = \hat{n}_1 - \hat{n}_2$ is a difference in electron density operator between two molecules constituting each dimer. $\tilde{g}_j$ is the ordinary EMV coupling constant of mode j defined as $\tilde{g}_j = \sqrt{\hbar/2\omega_j}\partial\epsilon_{\mathrm{HOMO}}/\partial Q_j$, where ϵ_{HOMO} is the energy of the highest occupied molecular orbital (HOMO), and Q_j is the normal coordinate. Comparing Eqs. (5) and (6), $\sigma(\omega) = \sigma_{\mathrm{d}}(\omega)$ is satisfied where the following two conditions are satisfied:

$$g_j = \tilde{g}_j \frac{|\langle E_+|\delta\hat{n}|E_-\rangle|}{\hbar} \sqrt{2\omega_{\mathrm{CT}}\omega_j},$$

$$\mu_{\mathrm{CT}} = ea|\langle E_+|\delta\hat{n}|E_-\rangle| \sqrt{\frac{N}{\Omega}\frac{\omega_{\mathrm{CT}}}{2\varepsilon_0\hbar}}. \quad (7)$$

Note that $\tilde{g}_j$ does not depend on the electronic state, but g_j depends on it. The above discussion shows that our phenomenological model is equivalent to the dimer model where Eqs. (7) hold and can represent a wider range of electronic states than the dimer model in which Eqs. (7) are not taken into account. This suggests that our model is a more general model in analyzing the optical spectra of the system constituting nonisolated dimers, as compared to the simple dimer model previously reported. In the quarter-filled systems such as $(\mathrm{TMTTF})_2\mathrm{PF}_6$, the infrared intensities of a_g phonon modes activated by the dimerization are considered to depend on the difference in the intensity between the intradimer and interdimer CT transitions [65], while the intradimer and interdimer transitions are not treated separately in our model as well as in the dimer model. In our model, that intensity difference between the intradimer and interdimer CT transitions can be incorporated by optimizing g_j without the restrictions of Eq. (7). This is advantageous for analyzing the electric field-induced spectral changes associated with a_g phonon modes, which occur because the displacements of two molecules in each dimer are modulated by the electric field via electron-lattice couplings and the intensities of a_g phonon modes are also changed.

TABLE I. Fitting parameters used for the simulation of reflectivity and optical conductivity spectra at 100 K shown by red lines in Figs. 3(a)–3(c).

ε_∞	$\hbar\omega_{\mathrm{CT}}$ (eV)	$\hbar\gamma_{\mathrm{CT}}$ (eV)	$\hbar\mu_{\mathrm{CT}}$ (eV)
1.76	0.155	0.14	0.96
j	$\hbar\omega_j$(eV)	$\hbar\gamma_j$(eV)	$\hbar^2 g_j$(eV^2)
1	0.162	1.50×10^{-2}	1.10×10^{-2}
2	0.135	9.05×10^{-4}	1.23×10^{-3}
3	0.114	9.07×10^{-4}	1.90×10^{-3}
4	0.053	2.00×10^{-3}	3.00×10^{-3}
5	0.039	3.79×10^{-3}	8.00×10^{-4}

Using Eq. (5), we fit the steady-state R and σ spectra. The fitting results are represented by red lines in Figs. 3(a)–3(f). The fitting parameters at 100 and 10 K are listed in Tables I and II, respectively. Both the broad spectral structure in the region above 0.2 eV and the complex structures below 0.2 eV are almost commonly reproduced at 100 and 10 K. The green lines in Figs. 3(b) and 3(c) and the blue lines in Figs. 3(e) and 3(f) represent the σ spectrum of the Lorentz oscillator of the CT transition alone. In Figs. 3(g) and 3(h), the spectral shape of the imaginary part of L_j is represented by the broken lines in a normalized scale, as well as the σ spectrum of the Lorentz oscillator of the CT transition by the green and blue lines, respectively, in an arbitrary unit. The red bars in Figs. 3(g) and 3(h) represent the magnitude of EMV coupling g_j of each intramolecular vibration. At 100 and 10 K, the frequencies of phonons hardly change, as listed in Tables I and II, and represented by the broken lines in Fig. 3(g) and 3(h). Concerning the frequencies and magnitudes of the EMV coupling constants of a_g modes in TMTTF molecules previously reported [29,66], we can correspondingly assign five oscillators (j = 1–5) to ν_4, ν_7, ν_8, ν_{10}, and ν_{11} modes, re-

TABLE II. Fitting parameters used for the simulation of reflectivity and optical conductivity spectra at 10 K shown by red lines in Figs. 3(d)–3(f).

ε_∞	$\hbar\omega_{\mathrm{CT}}$ (eV)	$\hbar\gamma_{\mathrm{CT}}$ (eV)	$\hbar\mu_{\mathrm{CT}}$ (eV)
1.68	0.128	0.084	0.905
j	$\hbar\omega_j$(eV)	$\hbar\gamma_j$(eV)	$\hbar^2 g_j$(eV^2)
1	0.165	2.88×10^{-2}	1.04×10^{-2}
2	0.135	9.05×10^{-4}	1.23×10^{-3}
3	0.114	9.07×10^{-4}	1.94×10^{-3}
4	0.052	4.30×10^{-3}	3.39×10^{-3}
5	0.039	3.79×10^{-3}	8.67×10^{-4}

spectively. This assignment is the same as that in the previous study at 300 K except for the presence of the ν_{11} mode [32]. By the introduction of EMV coupling and the resultant Fano interferences, the original σ spectra due to the CT transition (green and blue lines) are considerably changed with respect to the σ spectra represented by the red lines. In particular, a prominent change emerges as a dip structure around 0.17 eV at both 100 and 10 K, which is apparently due to the coupling of $a_g\nu_4$ mode with the CT transition.

Here, it is worth comparing the values of the ordinary EMV coupling constants $\tilde{g}_j$ obtained in our study with those previously reported. Using Eq. (7) and lattice parameters in Ref. [31], the parameters $\tilde{g}_j$ at 100 K are estimated to be $\tilde{g}_1 = 26.2$ meV, $\tilde{g}_2 = 3.2$ meV, $\tilde{g}_3 = 5.4$ meV, $\tilde{g}_4 = 12.5$ meV, and $\tilde{g}_5 = 3.9$ meV. In the previous study [32], $\tilde{g}_j$ $(j = 1{-}4)$ were estimated to be $\tilde{g}_1 = 37.2$ meV, $\tilde{g}_2 = 3.7$ meV, $\tilde{g}_3 = 9.3$ meV, and $\tilde{g}_4 = 24.8$ meV at 300 K using the simple dimer model. The relative magnitude ratios among the $\tilde{g}_j$ values in each evaluation are roughly the same with each other, while all the values of $\tilde{g}_j$ $(j = 1{-}4)$ at 100 K in our study are smaller than those at 300 K in the previous study [32]. The smaller values of $\tilde{g}_j$ $(j = 1{-}4)$ at 100 K relative to those at 300 K is attributable to the fact that the difference in the intradimer transfer integral t_1 and the interdimer transfer integral t_2 decreases with decrease of temperature [43]. The effect of the decrease in $(t_1 - t_2)$ on the a_g mode intensities cannot be taken into account in the simple dimer model and is reflected in the decrease in the absolute values of $\tilde{g}_j$ $(j = 1{-}4)$ at 100 K.

More strictly, there are finite differences between the experimental and calculated spectra, as shown in Fig. 3. Here, we briefly discuss the reasons for these differences. In dimerized quarter-filled systems, interdimer and intradimer transitions are sometimes clearly discriminated. For example, in a κ-type ET compound in the Mott-insulator phase, the interdimer transition is observed at lower energies than the intradimer transition [19,67]. In $(TMTTF)_2PF_6$, two types of transition bands would be superimposed in the measured energy region. In the present model, however, we assume that the CT transition is expressed by a single Lorentz oscillator, which might be the reason for the differences between the experimental and calculated spectra. As discussed in the following section, the spectral changes caused by the terahertz electric field pulse are almost reproduced from this model, assuming a single Lorentz oscillator as the CT transition. This can be attributed to the weakness of dimerization in $(TMTTF)_2PF_6$ compared to κ-type ET compounds. The validity of this simplification in dimerized molecular compounds with EMV couplings was also reported in the half-filled system such as K-TCNQ (TCNQ: tetracyanoquinodimethane) [65]. Thus, the proposed simplified model is suitable for analyzing both the steady-state and transient optical spectra in $(TMTTF)_2PF_6$.

D. Time evolution of reflectivity changes by a terahertz electric field pulse

In this subsection, we report the results of the terahertz pulse-pump optical-reflectivity probe measurements, which are illustrated in Fig. 5(a). First, we show the results of the time evolution of reflectivity changes, expressed as $\Delta R(t)/R$. In Fig. 5(b), we show the electric field waveform of a terahertz pump pulse, $E_{\mathrm{THz}}(t)$. The maximum electric field was approximately 300 kV/cm. The diameter of the probe pulse was 100 μm. This value was much smaller than the size of the ferroelectric domain, which was larger than 200 μm $\times$ 300 μm (see Sec. III A). Therefore, we could detect responses within a single ferroelectric domain. First, we set the probe energy at 0.65 eV. The electric fields of the terahertz pump pulse, E_{THz}, and the near-IR probe pulse, E, were both placed parallel to the a axis. Figures 5(c) and 5(d) depict the time evolution of $\Delta R(t)/R$ at 100 K in the Mott-insulator phase and at 10 K in the ferroelectric CO phase, respectively. At 100 K, the time evolution almost follows the square of $E_{\mathrm{THz}}(t)$ [red line in Fig. 5(c)], while at 10 K, $\Delta R(t)/R$ around the time origin follows $E_{\mathrm{THz}}(t)$ [red line in Fig. 5(d)]. At both temperatures, $\Delta R(t)/R$ seems to include coherent oscillations for $t > 0.7$ ps, which would be attributed to lattice modes in 1D TMTTF stacks.

To discuss the mechanism of the observed responses, we investigated how the magnitudes of the $\Delta R(t)/R$ signals depend on the electric field amplitude of the terahertz pulse. Figure 5(f) shows the dependence of $\Delta R(t)/R$ at the time origin, $\Delta R(0\ \mathrm{ps})/R$, on the maximum electric field, $|E_{\mathrm{THz}}(0\ \mathrm{ps})|$. The results clearly show that $\Delta R(0\ \mathrm{ps})/R$ is proportional to $|E_{\mathrm{THz}}(0\ \mathrm{ps})|$ at $T = 10$ K and to $|E_{\mathrm{THz}}(0\ \mathrm{ps})|^2$ at $T = 100$ K. These features can be explained in terms of system symmetry. In the ferroelectric CO phase at 10 K, the inversion symmetry is lost, as discussed in Sec. III A, so that the second-order nonlinear optical effect becomes active. By irradiating the crystal with the terahertz pump pulse and the near-IR probe pulse, the second-order nonlinear polarization $\Delta P^{(2)}$ expressed by the following formula emerges [68]:

$$\Delta P^{(2)}(\omega \pm \omega_{\mathrm{THz}}) = \varepsilon_0 \chi^{(2)} E_{\mathrm{THz}}(\pm\omega_{\mathrm{THz}}) E(\omega). \tag{8}$$

Here, ω_{THz} and ω are the frequencies of the terahertz pump pulse and the near-IR probe pulse, respectively. Given that $\omega_{\mathrm{THz}} \ll \omega$, we can consider that $\omega \pm \omega_{\mathrm{THz}} \simeq \omega$ and obtain the following relation:

$$\Delta P^{(2)}(\omega) = 2\varepsilon_0 \chi^{(2)} E_{\mathrm{THz}}(0) E(\omega). \tag{9}$$

This relation shows that the change in the complex dielectric constant, $\Delta\tilde{\varepsilon}$, is proportional to $E_{\mathrm{THz}}(t)$. Therefore, the reflectivity change is also proportional to $E_{\mathrm{THz}}(t)$ when the electric field is weak enough to neglect higher-order terms. At 100 K, the system presents inversion symmetry, and no second-order nonlinear optical effect exists. The lowest nonlinear optical effect is the third-order one. Using $\omega_{\mathrm{THz}} \ll \omega$, the third-order nonlinear polarization $\Delta P^{(3)}$ is expressed as follows [68]:

$$\Delta P^{(3)}(\omega) = 3\varepsilon_0 \chi^{(3)} E_{\mathrm{THz}}(0) E_{\mathrm{THz}}(0) E(\omega). \tag{10}$$

As a result, the reflectivity change is proportional to $|E_{\mathrm{THz}}(t)|^2$.

In the Mott-insulator phase at 100 K, a possible mechanism of third-order nonlinear optical response is the instability to the ferroelectric CO phase. In the Mott-insulator-to-ferroelectric-CO phase transition in $(TMTTF)_2PF_6$, structural changes are known to hardly occur, and the phase transition is electronic in nature. In other words, ferroelectricity is of

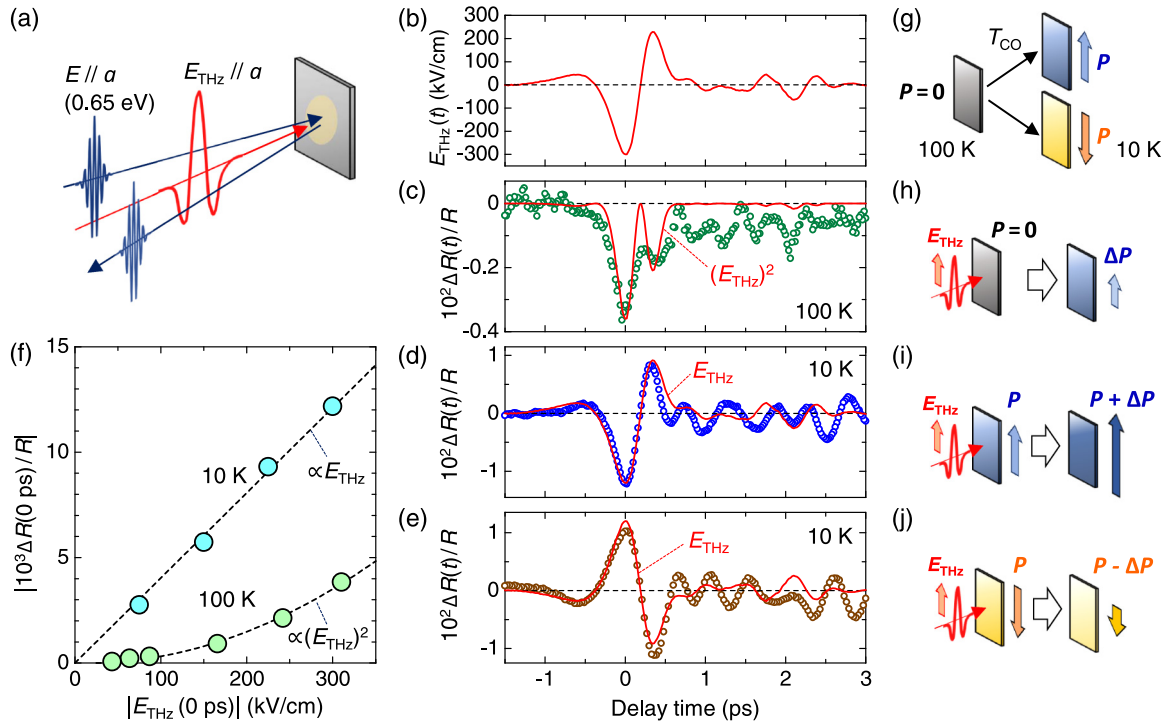

FIG. 5. (a) A schematic of the terahertz pulse-pump optical reflectivity probe measurements. (b) Electric field waveform of the terahertz pulse, $E_{\mathrm{THz}}(t)$. (c), (d) Time evolutions of electric field-induced reflectivity changes $\Delta R(t)/R$ at 0.65 eV in $(\mathrm{TMTTF})_2\mathrm{PF}_6$: (c) at 100 K and (d) at 10 K. (e) Time evolution of $\Delta R(t)/R$ at 10 K in a different sample from that in (d). (f) Magnitudes of $|\Delta R(0\ \mathrm{ps})/R|$ as a function of the electric field amplitude $|E_{\mathrm{THz}}(0\ \mathrm{ps})|$. (g)–(j) Schematics of polarization changes by the terahertz electric field: (h), (i), and (j) correspond to the results in (c), (d), and (e), respectively.

electronic type. Therefore, the electric field is expected to induce charge disproportionation in each dimer and generate a macroscopic polarization ΔP proportional to $E_{\mathrm{THz}}(t)$, as illustrated in Fig. 5(h). As a result, the third-order nonlinear optical response expressed in Eq. (8), or equivalently the $\Delta R(t)/R$ signals proportional to $|E_{\mathrm{THz}}(t)|^2$, emerge.

Regarding the ferroelectric phase at 10 K, in which the ionicity of charge-rich and charge-poor molecules are equal to $0.5+\delta$ and $0.5-\delta$, the original charge disproportionation should be modulated by the terahertz electric field. This induces a polarization change from the original value P to $P \pm \Delta P$ ($P, \Delta P > 0$). As a result, the second-order nonlinear optical response expressed in Eq. (7), or equivalently the $\Delta R(t)/R$ signals proportional to $E_{\mathrm{THz}}(t)$, emerge in the ferroelectric CO phase. Note that in Fig. 5(d), the sign of the signal of $\Delta R(t)/R$ at the time origin, $\Delta R(0\ \mathrm{ps})/R$, is the same as that in Fig. 5(c). In this case, it is expected that $E_{\mathrm{THz}}(t)$ at the time origin, $E_{\mathrm{THz}}(0\ \mathrm{ps})$, should be parallel to the macroscopic polarization P originating from the charge disproportionation, and that the charge disproportionation is enhanced and P is increased to $P+\Delta P$ at the time origin, as illustrated in Fig. 5(i).

Note that in a different crystal, we observed the $\Delta R(t)/R$ signal shown in Fig. 5(e), the sign of which is opposite to that of the $\Delta R(t)/R$ signal depicted in Fig. 5(d). In this case, $E_{\mathrm{THz}}(0\ \mathrm{ps})$ is antiparallel to P. The charge disproportionation is suppressed and P is decreased to $P-\Delta P$ at the time origin, as illustrated in Fig. 5(j), giving the opposite sign of $\Delta R/R(0\ \mathrm{ps})$. From these results, we conclude that the terahertz electric field modulates the ferroelectric polarization in $(\mathrm{TMTTF})_2\mathrm{PF}_6$, which is reflected by transient reflectivity changes.

E. Transient reflectivity spectrum in the Mott-insulator phase

To obtain information about the electronic-state changes caused by the terahertz electric field, we measured the spectrum of reflectivity changes. In this section, we report the results in the Mott-insulator phase at 100 K. Figure 6(b) shows the time evolution of $\Delta R(t)/R$ at 0.14, 0.7, and 0.32 eV as typical examples. The time profile of $|E_{\mathrm{THz}}(t)|^2$ is shown in Fig. 6(a). The maximum electric field was 300 kV/cm. The three $\Delta R(t)/R$ signals in Fig. 6(b) almost follow $|E_{\mathrm{THz}}(t)|^2$, while their magnitudes and signs depend on the probe energies. It is particularly characteristic that $\Delta R(t)/R$ around the time origin takes a large positive value (0.17 eV), in contrast to the negative small signals at higher (0.32 eV) and lower (0.14 eV) energies.

In Fig. 6(c), we plot the reflectivity change at the time origin, $\Delta R(0\ \mathrm{ps})$, represented by solid circles, for various probe energies. In the energy range of 0.15–0.2 eV, $\Delta R(0\ \mathrm{ps})$ shows a sharp positive structure peaked at 0.17 eV. For the rest of probe energies, $\Delta R(0\ \mathrm{ps})$ is negative and does not show prominent spectral structures. Figure 6(c) shows the steady-state R spectrum for comparison. At 0.17 eV, at which a peak of $\Delta R(0\ \mathrm{ps})$ exists, a dip structure is observed in the R spectrum that is ascribed to the presence of the $a_g\nu_4$ mode with a large EMV coupling constant, as discussed in Sec. III C

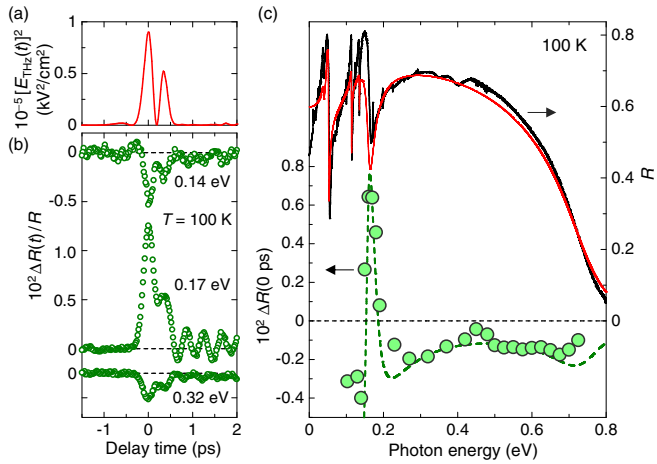

FIG. 6. (a) Time characteristic of $|E_{\mathrm{THz}}(t)|^2$. $E_{\mathrm{THz}}(t)$ is shown in Fig. 5(b). (b) Time evolutions of $\Delta R(t)/R$ at several typical probe energies at 100 K in $(TMTTF)_2PF_6$. (c) Probe-energy dependence of $\Delta R(0\ \mathrm{ps})$ at 100 K (green circles). The black and red solid lines show the steady-state R spectrum at 100 K and the simulated R spectrum, respectively. The green broken line shows the simulated ΔR spectrum (see the text).

[also see Fig. 3(g)]. Therefore, it is natural to consider that the peak structure in the $\Delta R(0\ \mathrm{ps})$ spectrum originates from the electric field-induced changes not only in the CT transition, but also from the coupling between this $a_g\nu_4$ mode and the CT transition. Therefore, we expect that we can reproduce the $\Delta R(0\ \mathrm{ps})$ spectrum by modifying the parameter values used in the analyses of the steady-state σ and R spectra in Sec. III C.

As discussed in Sec. III D, the electric field induces charge disproportionation in each dimer, which in turn causes some changes in the CT transition. Therefore, we set the CT transition energy, $\hbar\omega_{\mathrm{CT}}$, the damping constant, $\hbar\gamma_{\mathrm{CT}}$, and the parameter determining the transition dipole moment, $\hbar\mu_{\mathrm{CT}}$, to the fitting parameters. In general, it is natural to consider that $\hbar\gamma_{\mathrm{CT}}$ is unchanged by the electric field. However, as mentioned in Sec. III C, our model simply assumes a single Lorentz oscillator for the CT transition and does not consider the interdimer and intradimer transitions separately. By setting $\hbar\gamma_{\mathrm{CT}}$ as a fitting parameter, it may be possible to effectively capture complicated changes in both intradimer and interdimer transitions. At around 0.17 eV, where the $\Delta R(0\ \mathrm{ps})$ peak appears, no phonon modes exist except for $a_g\nu_4$ mode ($j = 1$); therefore, we consider only this mode for the analysis of the $\Delta R(0\ \mathrm{ps})$ spectrum. All the parameters of intramolecular vibrations, i.e., the frequency $\hbar\omega_j$, the damping constant, $\hbar\gamma_j$, and the EMV coupling constant, $\tilde{g}_j$, are characteristic of the TMTTF molecule itself, and they are independent of the electric field. However, g_j in our model depends on the electronic-state changes, and can be modulated by applying an external electric field. In the dimer limit (or equivalently a simple dimer model), the electric field-induced change in g_j, Δg_j, is one-to-one correspondence with the electric field-induced change in μ_{CT}, $\Delta\mu_{\mathrm{CT}}$, as $\Delta g_j/g_j = \Delta\mu_{\mathrm{CT}}/\mu_{\mathrm{CT}}$ derived from Eq. (7). However, as mentioned in Sec. III C, the dimeric molecular displacements can be modulated via electron-lattice coupling and the ratio of the intensities of the intradimer CT transition and the interdimer CT transition can be changed. This effect can be incorporated by setting Δg_j and $\Delta\mu_{\mathrm{CT}}$ as independent parameters. Briefly speaking, $\Delta\mu_{\mathrm{CT}}$ reflects the change in the sum of the intensities of the intradimer CT transition and the interdimer CT transition, while Δg_j reflects the change in the difference between them. To incorporate this effect into our model, we set $\hbar^2 g_1$ as a fitting parameter. To simplify the fitting analysis, we assume that the parameters $\hbar^2 g_2 - \hbar^2 g_5$ below 0.14 eV for a_g modes ($j = 2-5$) are unchanged. Thus, in our analysis, we attempted to fit the $\Delta R(0\ \mathrm{ps})$ spectrum from 0.14 to 0.72 eV by using four fitting parameters, namely $\hbar\omega_{\mathrm{CT}}$, $\hbar\gamma_{\mathrm{CT}}$, $\hbar\mu_{\mathrm{CT}}$, and $\hbar^2 g_1$.

The ΔR spectrum obtained by this fitting is represented by the broken line in Fig. 6(c), which reproduces the $\Delta R(0\ \mathrm{ps})$ spectrum (solid circles) experimentally obtained. As listed in Table III, the changes in the fitting parameters were the increase of $\hbar\omega_{\mathrm{CT}}$ by 4 meV (2.6%), the decrease of $\hbar\mu_{\mathrm{CT}}$ by 2 meV (0.21%), and the decrease of $\hbar^2 g_1$ by $0.045 \times 10^{-2}\ \mathrm{eV}^2$ (4.1%), while $\hbar\gamma_{\mathrm{CT}}$ remained unchanged. These changes in the parameters can be explained as follows: When an electric field is applied to a dimer in which the energies of two molecules are equivalent and charges are equally distributed to two molecules [Fig. 7(a)], a finite energy difference is induced between both molecules, and a charge disproportionation occurs [Fig. 7(b)]. In this case, energy splitting between the bonding and antibonding orbitals in the dimer increases, and the energy of the intradimer transition should increase, as shown in Fig. 7(b). The energy of the interdimer transition should also increase because of the increased energy splitting between the bonding and antibonding orbitals, although this transition is not explicitly considered in our model. The increase in the energy difference between the molecular orbitals of the neighboring molecules should suppress their effective hybridization and therefore decrease the dipole moment dominating the transition intensity. These discussions properly explain the increase of $\hbar\omega_{\mathrm{CT}}$ and the decrease of $\hbar\mu_{\mathrm{CT}}$ observed in the experiments. The decrease of $\hbar^2 g_1$ reflects the transfer of the spectral weight from the intradimer CT transition to the interdimer CT transition, which implies the

TABLE III. Fitting parameters used for the simulation of electric field-induced reflectivity change at 100 K shown by the green broken line in Fig. 6(c). Original parameters in the steady state, parameter values under the terahertz electric field, and their electric field-induced changes are listed.

	$\hbar\omega_{\mathrm{CT}}$ (eV)	$\hbar\gamma_{\mathrm{CT}}$ (eV)	$\hbar\mu_{\mathrm{CT}}$ (eV)	$\hbar^2 g_1$ (eV^2)
Steady state	0.155	0.14	0.960	1.100×10^{-2}
Under terahertz electric field	0.159	0.14	0.958	1.055×10^{-2}
Electric field-induced changes	0.004	0	−0.002	-0.045×10^{-2}

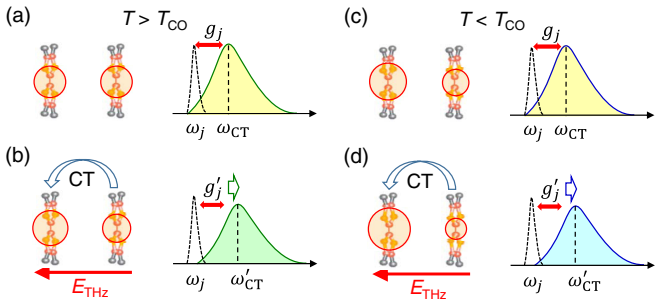

FIG. 7. Schematics of charge disproportionation and optical absorption spectra, and their electric field-induced changes: (a) at $T > T_{CO}$ and (c) at $T < T_{CO}$ in the steady states, and (b) at $T > T_{CO}$ and (d) at $T < T_{CO}$ under electric fields. Colored solid and black dotted lines in the right part of each figure show the absorption spectra of the CT band and a_g mode, respectively. The increase of the charge disproportionation induces the blueshift of the CT band and weakens the EMV coupling characterized by g_j.

weakening of the dimerization. In fact, if $\hbar^2 g_1$ is not a fitting parameter, $\Delta R(0\ \mathrm{ps})$ spectrum cannot be reproduced. These changes of the parameters are reasonable because the charge disproportionation is created and the energy gain by forming bonding orbital in each dimer is expected to decrease when the terahertz electric field is applied. From these considerations, the spectrum of reflectivity changes can be interpreted by the charge disproportionation within each dimer and the weakening of the dimerization caused by the electric field.

F. Transient reflectivity spectrum in the CO phase

In this section, we report the spectrum of $\Delta R(0)$ in the polar CO phase at 10 K. Figure 8(b) shows the time evolution of $\Delta R(t)/R$ at 0.14, 0.17, and 0.32 eV as typical examples. The electric field waveform of $E_{THz}(t)$ is shown in Fig. 8(a). The

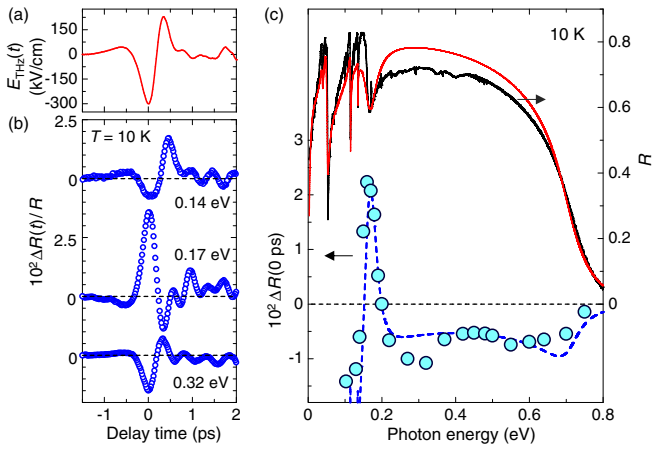

FIG. 8. (a) Electric field waveform of the terahertz pump pulse, $E_{THz}(t)$ [the same as that shown in Fig. 5(b)]. (b) Time evolutions of $\Delta R(t)/R$ at several typical probe energies at 10 K in $(TMTTF)_2PF_6$. (c) Probe-energy dependence of $\Delta R(0\ \mathrm{ps})$ at 10 K (blue circles). The black and red solid lines show the steady-state R spectrum at 10 K and the simulated R spectrum, respectively. The blue broken line shows the simulated ΔR spectrum (see the text).

maximum electric field was approximately 300 kV/cm. The time characteristics of the three $\Delta R(t)/R$ signals in Fig. 8(b) are almost proportional to $E_{THz}(t)$, while their magnitudes and signs depend on the probe energies. Similar to the results at 100 K, $\Delta R(0\ \mathrm{ps})/R$ at the time origin takes a large value (0.17 eV) compared with that at higher (0.32 eV) and lower (0.14 eV) energies. In addition, the sign of $\Delta R(0\ \mathrm{ps})/R$ at 0.17 eV is positive, while that at 0.14 and 0.32 eV is negative.

Figure 8(c) shows the reflectivity change at the time origin, $\Delta R(0\ \mathrm{ps})$, represented by solid circles for several probe energies. In the energy range of 0.15–0.2 eV, $\Delta R(0\ \mathrm{ps})$ shows a sharp positive structure peaked at 0.17 eV, similar to the $\Delta R(0\ \mathrm{ps})$ spectrum at 100 K. This dip is also ascribed to the presence of the $a_g \nu_4$ mode with a large EMV coupling constant, as discussed in Sec. III C [see Fig. 3(h)]. Concerning the rest of probe energies, $\Delta R(0\ \mathrm{ps})$ is negative and does not show prominent structures. Figure 8(c) depicts the steady-state R spectrum for comparison. At 0.17 eV, at which a peak of $\Delta R(0\ \mathrm{ps})$ exists, a dip structure due to the coupling of a_g mode 1 with the CT transition is observed in the R spectrum. Therefore, it is natural to relate the sharp peak of $\Delta R(0\ \mathrm{ps})$ at 0.17 eV to $a_g \nu_4$ mode ($j = 1$) of the intramolecular vibration, similar to the case at 100 K. We also performed a fitting analysis of the $\Delta R(0\ \mathrm{ps})$ spectrum by setting $\hbar\omega_{CT}$, $\hbar\gamma_{CT}$, $\hbar\mu_{CT}$, and $\hbar^2 g_1$ as the fitting parameters. The other parameters were fixed to those used in the fitting of the steady-state spectra, as shown in Table II.

The ΔR spectrum obtained by the fitting is represented by the broken line in Fig. 8(c), which reproduces the $\Delta R(0\ \mathrm{ps})$ spectrum (solid circles) experimentally obtained. As listed in Table IV, the changes in the fitting parameters were the increase of $\hbar\omega_{CT}$ by 10 meV (7.8%), the decrease of $\hbar\mu_{CT}$ by 3 meV (0.3%), the increase $\hbar\gamma_{CT}$ by 1.5 meV (1.8%), and the decrease of $\hbar^2 g_1$ by 0.135×10^{-2} eV^2 (13.0%). The tendency of the changes in $\hbar\omega_{CT}$, $\hbar\mu_{CT}$, and $\hbar^2 g_1$ are qualitatively the same as those observed in the Mott-insulator phase (Table III). Therefore, in the polar CO phase, we can consider that the charge disproportionation in the steady state is enhanced by the electric field. This results in the increase of $\hbar\omega_{CT}$ and the decrease of $\hbar\mu_{CT}$. These responses are illustrated in Figs. 7(c) and 7(d). We also comment on the slight increase in $\hbar\gamma_{CT}$. As mentioned above, we used a single Lorentz oscillator for the CT transition, and the intradimer and interdimer transitions were not discriminated. If the increases in the energies of two CT transitions by the electric field are different from each other, it might be reflected by the increase of $\hbar\gamma_{CT}$.

G. Coherent oscillations on reflectivity changes

Figures 5(d), 5(e) and 8(b) show, in the polar CO phase, oscillatory components that remain on the reflectivity changes for $t_d > 1$ ps after the electric field of the pump pulse almost diminishes. At 100 K, in the Mott-insulator phase, some oscillatory components also seem to exist [see Figs. 5(c) and 6(b)], although their intensities are relatively small compared to those at 10 K. Figures 9(b) and 9(c) show the Fourier power spectra of $\Delta R/R(t)$ at 0.65 eV at 10 K [Fig. 5(e)] and 100 K [Fig. 5(c)], respectively. They were obtained by calculating the Fourier transform of $\Delta R/R$ in the range from 0.8 to 30 ps. The red line in Fig. 9(a) depicts the

TABLE IV. Fitting parameters used for the simulation of electric field-induced reflectivity change at 10 K shown by the blue broken line in Fig. 8(c). Original parameters in the steady state, parameter values under the terahertz electric field, and their electric field-induced changes are listed.

	$\hbar\omega_{CT}$ (eV)	$\hbar\gamma_{CT}$ (eV)	$\hbar\mu_{CT}$ (eV)	$\hbar^2 g_1$ (eV^2)
Steady state	0.128	0.0840	0.905	1.040×10^{-2}
Under terahertz electric field	0.138	0.0855	0.902	0.905×10^{-2}
Electric field-induced changes	0.010	0.0015	−0.003	-0.135×10^{-2}

Fourier power spectrum of the terahertz pump pulse, as shown in Fig. 5(b).

At 10 K in the polar CO phase, a strong peak is observed at 42 cm^{-1} in the Fourier power spectrum in Fig. 9(b). This frequency almost coincides with that of a librational or internal mode of the $(TMTTF)_2^+$ dimer observed through Raman spectroscopy [29]; IR spectroscopy was not performed below 45 cm^{-1}. This Raman-active mode can also become IR active in the CO phase because of charge disproportionation, or equivalently breaking of the inversion symmetry. Therefore, this mode might be resonantly excited by the terahertz electric field and generate a strong coherent oscillation of the reflectivity changes. In addition to this peak, several weak peaks are identified in the range from 50 to 90 cm^{-1}, although their frequencies are difficult to be determined accurately because of the poor frequency resolution in our data. Previous IR spectroscopy revealed that several vibrational modes exist in this frequency region in the CO phase; they are assigned to translational and internal modes, such as the boat mode [29].

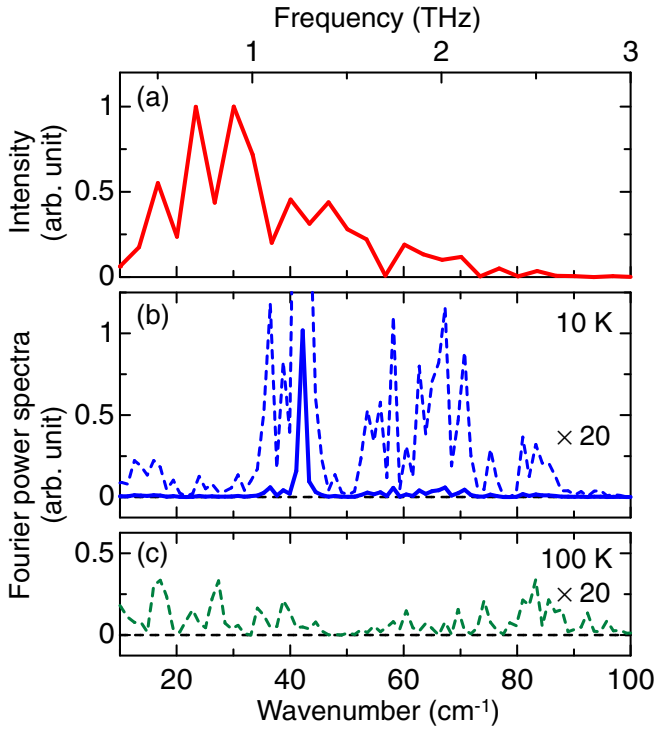

FIG. 9. (a) Fourier power spectrum of an electric field waveform of a terahertz pump pulse shown in Fig. 5(b). (b), (c) Fourier power spectra of oscillatory components on $\Delta R(t)/R$ shown in Fig. 5(d) at 10 K and in Fig. 5(c) at 100 K. The spectra in (b), (c) are obtained by the $\Delta R(t)/R$ data in the range of 0.8–30 ps.

Some of these modes are Raman active and IR inactive in the Mott-insulator phase, but become IR active in the CO phase. The weak peaks observed in Fig. 9(b) might be ascribed to the IR-active modes excited by the terahertz electric field.

Several peak structures are observed in the Fourier power spectrum at 100 K in the Mott-insulator phase, as shown in Fig. 9(c). However, their intensities were relatively smaller than those of the peak structures observed in the CO phase [Fig. 9(b)]. As mentioned above, most of the modes observed from 50 to 90 cm^{-1} are IR active in the CO phase, while they are expected to be IR inactive in the Mott-insulator phase and cannot be directly excited by the terahertz electric field. According to Ref. [29], the terahertz electric field cannot excite lattice modes except for an antiphase librational mode around the a axis in the Mott-insulator phase, which was derived through symmetry analysis. This is the reason why the intensities of the coherent oscillations are weak in the Mott-insulator phase. The weak oscillations observed in this phase are attributable to molecular oscillations driven by the electric field-induced charge modulation. Besides, in the Mott-insulator phase, the terahertz electric field gives rise to a potential difference between two molecules in each dimer. Then the energy gain by forming bonding orbital decreases in proportion to E_{THz}^2, which results in an external force proportional to E_{THz}^2 applied to the dimerization mode. Thus each molecule subsequently moves to decrease the dimerization. These molecular motions may be observed as coherent oscillations. As seen in Fig. 9(c), the coherent oscillation at around 83 cm^{-1} is relatively strong in the Mott-insulator phase and its intensity is comparable to that observed in the CO phase. Considering that the intensity of the terahertz pump pulse is negligibly small in this frequency region above 80 cm^{-1}, this mode with 83 cm^{-1} would be driven not by the direct excitation with the terahertz pulse but by the electric field-induced charge disproportionation. This interpretation is reasonable because the mode at 83 cm^{-1} was assigned to the antiphase translation along the a axis within the dimer in previous vibrational spectroscopy studies [29].

H. Temperature dependence of reflectivity changes

Finally, we report the temperature dependence of electric field-induced reflectivity changes, i.e., $\Delta R(t)/R$. The data were taken in a different crystal with respect to that used in the measurements shown in Figs. 5, 6, 8, and 9. As mentioned in Sec. III D, the sign of reflectivity changes depends on the direction of the electric field of the terahertz pump pulse relative to the original polarization P. In the crystal used, the sign of $\Delta R(0\text{ ps})/R$ (0.65 eV) at 10 K is negative, indicating that the

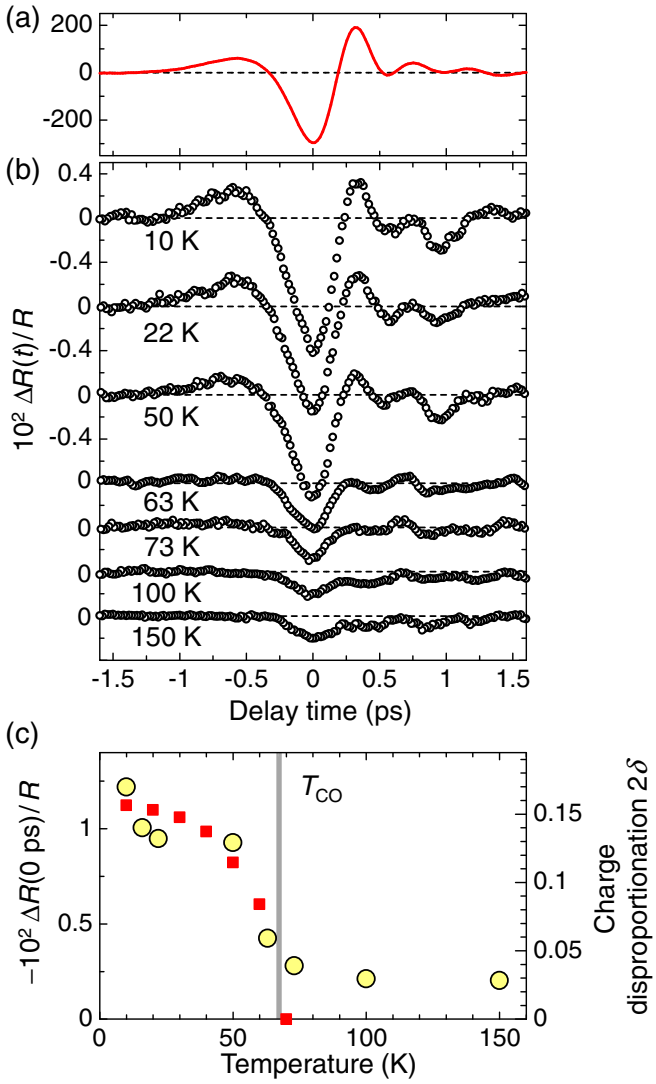

FIG. 10. (a) Electric field waveform of the terahertz pump pulse, $E_{\mathrm{THz}}(t)$. (b) Time evolutions of $\Delta R(t)/R$ at 0.65 eV at various temperatures in $(TMTTF)_2PF_6$. (c) Temperature dependence of $-\Delta R(0\ \mathrm{ps})/R$ (yellow circles). The gray line shows the Mott-insulator to charge-order insulator transition temperature T_{CO}. Red squares show the magnitudes of charge disproportionation, 2δ, evaluated by the molecular vibrational spectroscopy [29].

terahertz electric field is parallel to the original polarization, and the condition is the same as that in Figs. 5(d) and 8.

Figure 10(a) shows the electric field waveform of the terahertz pulse, $E_{\mathrm{THz}}(t)$, used in this experiment, which is almost the same as that depicted in Fig. 5(b). The maximum electric field was approximately 300 kV/cm. Figure 10(b) shows the time evolution of $\Delta R(t)/R$ at 0.65 eV and different temperatures. Below $T_{CO} = 67$ K, $\Delta R(t)/R$ is almost proportional to $E_{\mathrm{THz}}(t)$, whereas above T_{CO}, it is almost proportional to $|E_{\mathrm{THz}}(t)|^2$. Below and above T_{CO}, the $\Delta R(t)/R$ signals almost disappear for $t_d > 1$ ps when the terahertz electric field diminishes, except for the residual coherent oscillations discussed in Sec. III G. The time characteristics of $\Delta R(t)/R$ remain almost unchanged between 50 and 10 K, suggesting that the CO pattern is also unchanged across the spin-Peierls transition at $T_{SP} = 19$ K. This is consistent with a previous detailed x-ray diffraction study [31]. Above T_{CO}, the time characteristics of $\Delta R(t)/R$ do not depend significantly on the temperature. No critical behavior appears in the responses to the terahertz electric field near T_{CO}. These results suggest that the observed responses are dominated mainly by the charge modulations induced by the terahertz electric field. The observation of coherent oscillations shows the presence of the coupling of the charge sector with some lattice modes. The charge sector might also be coupled with the displacement of anions, as previously reported [69]. However, considering that the time characteristics of $\Delta R(t)/R$ almost follow $E_{\mathrm{THz}}(t)$ below T_{CO} and $|E_{\mathrm{THz}}(t)|^2$ above T_{CO}, and that delayed responses are hardly observed, the contributions of the electron-lattice coupling to the overall responses are not significant. This corresponds to the fact that the structural change across T_{CO} is small and the CO state below T_{CO} has an electronic origin, that is, the intermolecular Coulomb interaction.

It is important to comment on the effects of intramolecular vibrations. The frequency of our electric field pulse was approximately 1 THz or 30 cm^{-1}, so that most of the intramolecular vibrational modes could follow the electric field. In this case, the time evolution of $\Delta R(t)/R$ should reflect not only the dynamics of the charge sector but also the structural changes associated with intramolecular vibrations, such as deformation, shrinking, and expansion of molecules. In the time evolution of $\Delta R(t)/R$, we cannot discriminate the contribution of molecular dynamics by the electric field from that of charge dynamics. However, in our study, we succeeded in revealing the contribution of the EMV coupling to the responses to the electric field from the analysis of the $\Delta R(0\ \mathrm{ps})$ spectra, as discussed in Secs. III E and III F. The results suggest that the EMV coupling is important and that the intramolecular structural dynamics play important roles in the responses to the electric field in $(TMTTF)_2PF_6$.

Figure 10(c) depicts the values of $-\Delta R(0\ \mathrm{ps})/R$ at 0.65 eV represented by yellow circles as a function of temperature. Below T_{CO}, $-\Delta R(0\ \mathrm{ps})/R$ increases with a decrease in temperature. It is valuable to compare this temperature dependence with that of the amplitude of the original CO or, equivalently, the charge disproportionation magnitude 2δ. The temperature dependence of 2δ was previously reported from the splitting of the intramolecular vibration frequencies, which sensitively changed depending on the molecular ionicity [29]. Figure 10(c) shows the temperature dependence of 2δ evaluated by the red squares. The temperature dependences of $-\Delta R(0\ \mathrm{ps})/R$ and 2δ are roughly the same. This tendency is reasonable by considering three plausible relations: (1) $\Delta R(0\ \mathrm{ps})/R$ is proportional to $\chi^{(2)}E_{\mathrm{THz}}(0)$ (see Sec. III D), (2) $\chi^{(2)}$ is proportional to the macroscopic polarization P, and (3) P is proportional to 2δ. To induce more drastic changes in the electronic states, such as the electric field-induced transitions between the CO-insulator phase and the Mott-insulator phase [19], or from the CO-insulator (Mott-insulator) phase to metal [10], a more intense electric field is necessary.

IV. SUMMARY

We investigated the electronic-state changes caused by a strong electric field in an organic molecular compound,

$(TMTTF)_2PF_6$, using terahertz pulse-pump optical-reflectivity probe spectroscopy. We observed reflectivity changes proportional to the square of the electric field waveform of the terahertz pulse in the Mott-insulator phase and also reflectivity changes proportional to the electric field waveform in the charge-order insulator phase. These different responses are ascribed to the difference in the symmetry of the electronic states; the inversion symmetry exists in the Mott-insulator phase and is lost in the charge-order phase. The electric field-induced change in the optical-reflectivity spectrum can be attributed to the change in the charge disproportionation in each dimer and the weakening of the dimerization by the electric field. In the Mott-insulator phase, the electric field generates charge disproportionation, whereas in the charge-order phase, it modulates the original charge disproportionation. In the mid-IR region, where intramolecular a_g-mode vibrations coupled with intermolecular electron transfers exist, the electric field-induced reflectivity changes are considerably enhanced. To interpret this feature, we constructed a model that incorporates a charge-transfer transition and intramolecular a_g-modes vibrations. This model encompasses a simple dimer model, and can also incorporate the effect of the interdimer CT transition, which cannot be captured by a simple dimer model. The analyses with this model revealed that the electric field-induced change in the reflectivity spectrum can be explained by the energy shift of the overall CT transition and the changes in the dipole moments of both the intradimer and interdimer CT transitions, which are caused by the change in the charge disproportionation in each dimer, and the transfer of the spectral weight between the intradimer and interdimer CT transitions due to the changes of the dimeric molecular displacements. Our approach encompasses the pump-probe experiments using terahertz electric field pulses, and simulations of spectral changes using the effective classical model, which can be used to analyze optical responses to an electric field in various organic molecular compounds with EMV couplings.

ACKNOWLEDGMENTS

This work was partly supported by Grants-in-Aid for Scientific Research from the Japan Society for the Promotion of Science (JSPS) (Projects No. JP18H01166, No. JP18H01858, No. JP20K03801, and No. JP21H04988) and by Core Research for Evolutional Science and Technology (CREST) (Grant No. JPMJCR1661), Japan Science and Technology Agency. H.Y., T. Morimoto, and T.O. were supported by the JSPS through the Program for Leading Graduate Schools (MERIT). H.Y. and T. Morimoto were supported by JSPS Research Fellowships for Young Scientists.

[1] J. Hebling, G. Almási, I. Z. Kozma, and J. Kuhl, Velocity matching by pulse front tilting for large-area THz-pulse generation, Opt. Express **10**, 1161 (2002).

[2] T. Kampfrath, K. Tanaka, and K. A. Nelson, Resonant and nonresonant control over matter and light by intense terahertz transients, Nat. Photonics **7**, 680 (2013).

[3] I. Katayama, H. Aoki, J. Takeda, H. Shimosato, M. Ashida, R. Kinjo, I. Kawayama, M. Tonouchi, M. Nagai, and K. Tanaka, Ferroelectric Soft Mode in a $SrTiO_3$ Thin Film Impulsively Driven to the Anharmonic Regime Using Intense Picosecond Terahertz Pulses, Phys. Rev. Lett. **108**, 097401 (2012).

[4] T. Kampfrath, A. Sell, G. Klatt, A. Pashkin, S. Mährlein, T. Dekorsy, M. Wolf, M. Fiebig, A. Leitenstorfer, and R. Huber, Coherent terahertz control of antiferromagnetic spin waves, Nat. Photonics **5**, 31 (2011).

[5] T. Kubacka, J. A. Johnson, M. C. Hoffmann, C. Vicario, S. de Jong, P. Beaud, S. Grübel, S.-W. Huang, L. Huber, L. Patthey, Y.-D. Chuang, J. J. Turner, G. L. Dakovski, W.-S. Lee, M. P. Minitti, W. Schlotter, R. G. Moore, C. P. Hauri, S. M. Koohpayeh, V. Scagnoli, G. Ingold, S. L. Johnson, and U. Staub, Large-amplitude spin dynamics driven by a THz pulse in resonance with an electromagnon, Science **343**, 1333 (2014).

[6] H. Hirori, M. Nagai, and K. Tanaka, Excitonic interactions with intense terahertz pulses in ZnSe/ZnMgSSe multiple quantum wells, Phys. Rev. B **81** 081305(R) (2010).

[7] T. Terashige, T. Ono, T. Miyamoto, T. Morimoto, H. Yamakawa, N. Kida, T. Ito, T. Sasagawa, T. Tohyama, and H. Okamoto, Doublon-holon pairing mechanism via exchange interaction in two-dimensional cuprate Mott insulators, Sci. Adv. **5**, eaav2187 (2019).

[8] T. Miyamoto, T. Kakizaki, T. Terashige, D. Hata, H. Yamakawa, T. Morimoto, N. Takamura, H. Yada, Y. Takahashi, T. Hasegawa, H. Matsuzaki, T. Tohyama, and H. Okamoto, Biexciton in one-dimensional Mott insulators, Commun. Phys. **2**, 131 (2019).

[9] M. Liu, H. Y. Hwang, H. Tao, A. C. Strikwerda, K. Fan, G. R. Keiser, A. J. Sternbach, K. G. West, S. Kittiwatanakul, J. Lu, S. A. Wolf, F. G. Omenetto, X. Zhang, K. A. Nelson, and R. D. Averitt, Terahertz-field-induced insulator-to-metal transition in vanadium dioxide metamaterial, Nature (London) **487**, 345 (2012).

[10] H. Yamakawa, T. Miyamoto, T. Morimoto, T. Terashige, H. Yada, N. Kida, M. Suda, H. M. Yamamoto, R. Kato, K. Miyagawa, K. Kanoda, and H. Okamoto, Mott transition by an impulsive dielectric breakdown, Nat. Mater. **16**, 1100 (2017).

[11] T. Miyamoto, H. Yada, H. Yamakawa, and H. Okamoto, Ultrafast modulation of polarization amplitude by terahertz fields in electronic-type organic ferroelectrics, Nat. Commun. **4**, 2586 (2013).

[12] F. Chen, J. Goodfellow, S. Liu, I. Grinberg, M. C. Hoffmann, A. R. Damodaran, Y. Zhu, P. Zalden, X. Zhang, I. Takeuchi, A. M. Rappe, L.W. Martin, H. Wen, and A.M. Lindenberg, Ultrafast terahertz gating of the polarization and giant nonlinear optical response in $BiFeO_3$ thin films, Adv. Mater. **27**, 6371 (2015).

[13] Y. Okimoto, S. Naruse, R. Fukaya, T. Ishikawa, S. Koshihara, K. Oka, M. Azuma, K. Tanaka, and H. Hirori, Ultrafast Control of the Polarity of $BiCoO_3$ by Orbital Excitation as Investigated by Femtosecond Spectroscopy, Phys. Rev. Appl. **7**, 064016 (2017).

[14] X. Li, T. Qiu, J. Zhang, E. Baldini, J. Lu, A. M. Rappe, and K. A. Nelson, Terahertz field–induced ferroelectricity in quantum paraelectric $SrTiO_3$, Science **364**, 1079 (2019).

[15] H. Yamakawa, T. Miyamoto, T. Morimoto, H. Yada, Y. Kinoshita, M. Sotome, N. Kida, K. Yamamoto, K. Iwano, Y. Matsumoto, S. Watanabe, Y. Shimoi, M. Suda, H. M. Yamamoto, H. Mori, and H. Okamoto, Novel electronic

ferroelectricity in an organic charge-order insulator investigated with terahertz-pump optical-probe spectroscopy, Sci. Rep. **6**, 20571 (2016).

[16] T. Morimoto, T. Miyamoto, H. Yamakawa, T. Terashige, T. Ono, N. Kida, and H. Okamoto, Terahertz-Field-Induced Large Macroscopic Polarization and Domain-Wall Dynamics in an Organic Molecular Dielectric, Phys. Rev. Lett. **118**, 107602 (2017).

[17] T. Miyamoto, D. Hata, T. Morimoto, H. Yamakawa, N. Kida, T. Terashige, K. Iwano, H. Kishida, S. Horiuchi, and H. Okamoto, Ultrafast polarization control by terahertz fields via π-electron wavefunction changes in hydrogen-bonded molecular ferroelectrics, Sci. Rep. **8**, 15014 (2018).

[18] T. Miyamoto, H. Yamakawa, T. Morimoto, and H. Okamoto, Control of electronic states by a nearly monocyclic terahertz electric-field pulse in organic correlated electron materials, J. Phys. B: At. Mol. Opt. Phys. **51**, 162001 (2018).

[19] H. Yamakawa, T. Miyamoto, T. Morimoto, N. Takamura, S. Liang, H. Yoshimochi,T. Terashige, N. Kida, M. Suda, H. M. Yamamoto, H. Mori, K. Miyagawa, K. Kanoda, and H. Okamoto, Terahertz-field-induced polar charge order in electronic-type dielectrics, Nat. Commun. **12**, 953 (2021).

[20] K. Yamamoto, S. Iwai, S. Boyko, A. Kashiwazaki, F. Hiramatsu, C. Okab, N. Nishi, and K. Yakushi, Strong optical nonlinearity and its ultrafast response associated with electron ferroelectricity in an organic conductor, J. Phys. Soc. Jpn. **77**, 074709 (2008).

[21] K. Kobayashi, S. Horiuchi, R. Kumai, F. Kagawa, Y. Murakami, and Y. Tokura, Electronic Ferroelectricity in a Molecular Crystal with Large Polarization Directing Antiparallel to Ionic Displacement, Phys. Rev. Lett. **108**, 237601 (2012).

[22] J. B. Torrance, A. Girlando, J. J. Mayerle, J. I. Crowley, V. Y. Lee, P. Batail, and S. J. LaPlaca, Anomalous Nature of Neutral-to-Ionic Phase Transition in Tetrathiafulvalene-Chloranil, Phys. Rev. Lett. **47**, 1747 (1981).

[23] H. Okamoto, T. Mitani, Y. Tokura, S. Koshihara, T. Komatsu, Y. Iwasa, T. Koda, and G. Saito, Anomalous dielectric response in tetrathiafulvalene-p-chloranil as observed in temperature- and pressure-induced neutral-to-ionic phase transition, Phys. Rev. B **43**, 8224 (1991).

[24] M. Le Cointe, M. H. Lemée-Cailleau, H. Cailleau, B. Toudic, L. Toupet, G. Heger, F. Moussa, P. Schweiss, K. H. Kraft, and N. Karl, Symmetry breaking and structural changes at the neutral-to-ionic transition in tetrathiafulvalene-p-chloranil, Phys. Rev. B **51**, 3374 (1995).

[25] G. Giovannetti, S. Kumar, A. Stroppa, J. V. D. Brink, and S. Picozzi, Multiferroicity in TTF-CA Organic Molecular Crystals Predicted through Ab Initio Calculations, Phys. Rev. Lett. **103**, 266401 (2009).

[26] S. Ishibashi and K. Terakura, Exotic ferroelectricity in tetrathiafulvalene-*p*-Chloranil: Anomalous effective charges and a picture in the framework of maximally localized Wannier orbitals, J. Phys. Soc. Jpn. **83**, 073702 (2014).

[27] T. Kakiuchi, Y. Wakabayashi, H. Sawa, T. Takahashi, and T. Nakamura, Charge ordering in α-(BEDT-TTF)$_2$I$_3$ by synchrotron x-ray diffraction, J. Phys. Soc. Jpn. **76**, 113702 (2007).

[28] D. Jérome, The physics of organic superconductors, Science **252**, 1509 (1991).

[29] M. Dressel, M. Dumm, T. Knoblauch, and M. Masino, Comprehensive optical investigations of charge order in organic chain compounds (TMTTF)$_2$X, Crystals **2**, 528 (2012).

[30] G. Brun, B. Liautard, S. Peytavin, and M. Maurin, Sels du radical cationique TMTTF (Tétraméthyltétrathiofulvalène). Structures et propriétés, J. Phys. (Paris), Colloq. **38**, C7-266 (1977).

[31] S. Kitou, T. Fujii, T. Kawamoto, N. Katayama, S. Maki, E. Nishibori, K. Sugimoto, M. Takata, T. Nakamura, and H. Sawa, Successive Dimensional Transition in (TMTTF)$_2$PF$_6$ Revealed by Synchrotron X-ray Diffraction, Phys. Rev. Lett. **119**, 065701 (2017).

[32] C. S. Jacobsen, D. B. Tanner, and K. Bechgaard, Optical and infrared properties of tetramethyltetraselenafulvalene [(TMTSF)$_2$X] and tetramethyltetrathiafulvalene [(TMTTF)$_2$X] compounds, Phys. Rev. B **28**, 7019 (1983).

[33] D. Jérome, Organic superconductors, Solid State Commun. **92**, 89 (1994).

[34] D. Jérome, P. AubanSenzier, L. Balicas, K. Behnia, W. Kang, P. Wzietek, C. Berthier, P. Caretta, M. Horvatic, P. Segransa, L. Hubert, and C. Bourbonnais, (TM)$_2$X organic superconductors: Interplay between 1-D charge localization and higher dimensionality cross-over, Synth. Met. **70**, 719 (1995).

[35] V. Vescoli, L. Degiorgi, W. Henderson, G. Grüner, K. P. Starkey, and L. K. Montgomery, Dimensionality-driven insulator-to-metal transition in the Bechgaard salts, Science **281**, 1181 (1998).

[36] P. Monceau, F. Ya. Nad, and S. Brazovskii, Ferroelectric Mott-Hubbard Phase of Organic (TMTTF)$_2$X Conductors, Phys. Rev. Lett. **86**, 4080 (2001).

[37] H. Seo and H. Fukuyama, Antiferromagnetic phases of one-dimensional quarter-filled organic conductors, J. Phys. Soc. Jpn. **66**, 1249 (1997).

[38] S. Mazumdar, R. T. Clay, and D. K. Campbell, Bond-order and charge-density waves in the isotropic interacting two-dimensional quarter-filled band and the insulating state proximate to organic superconductivity, Phys. Rev. B **62**, 13400 (2000).

[39] Y. Shibata, S. Nishimoto, and Y. Ohta, Charge ordering in the one-dimensional extended Hubbard model: Implication to the TMTTF family of organic conductors, Phys. Rev. B **64**, 235107 (2001).

[40] B. Kohler, E. Rose, M. Dumm, G. Untereiner, and M. Dressel, Comprehensive transport study of anisotropy and ordering phenomena in quasi-one-dimensional (TMTTF)$_2$X salts (X = PF$_6$, AsF$_6$, SbF$_6$, BF$_4$, ClO$_4$, ReO$_4$), Phys. Rev. B **84**, 035124 (2011).

[41] D. S. Chow, F. Zamborszky, B. Alavi, D. J. Tantillo, A. Baur, C. A. Merlic, and S. E. Brown, Charge Ordering in the TMTTF Family of Molecular Conductors, Phys. Rev. Lett. **85**, 1698 (2000).

[42] T. Nakamura, K. Furukawa, and T. Hara, Redistribution of charge in the proximity of the spin-Peierls transition: ^{13}C NMR investigation of (TMTTF)$_2$PF$_6$, J. Phys. Soc. Jpn. **76**, 064715 (2007).

[43] S. Kitou, L. Zhang, T. Nakamura, and H. Sawa, Complex changes in structural parameters hidden in the universal phase diagram of the quasi-one-dimensional organic conductors (TMTTF)$_2$X (X = NbF$_6$, AsF$_6$, PF$_6$, and Br), Phys. Rev. B **103**, 184112 (2021).

[44] M. J. Rice, Organic Linear Conductors as Systems for Study of Electron-Phonon Interactions in Organic Solid-State, Phys. Rev. Lett. **37**, 390 (1976).

[45] M. J. Rice, L. Pietronero, and P. Brüesch, Phase phonons and intramolecular electron-phonon coupling in organic linear-chain semiconductor TEA(TCNQ)$_2$, Solid State Commun. **21**, 757 (1977).

[46] M. J. Rice, N. O. Lipari, and S. Strässler, Dimerized Organic Linear-Chain Conductors and Unambiguous Experimental-Determination of Electron-Molecular-Vibration Coupling-Constants. Phys. Rev. Lett. **39**, 1359 (1977).

[47] M. J. Rice, Towards the experimental determination of the fundamental microscopic parameters of organic ion-radical compounds, Solid State Commun. **31**, 93 (1979).

[48] M. J. Rice, V. M. Yartsev, and C. S. Jacobsen, Investigation of the nature of the unpaired electron states in the organic semiconductor N-methyl-N-ethylmorpholinium-tetracyanoquinodimethane, Phys. Rev. B **21**, 3437 (1980).

[49] T. Nakamura, Possible charge ordering patterns of the paramagnetic insulating states in (TMTTF)$_2$X, J. Phys. Soc. Jpn. **72**, 213 (2003).

[50] M. Sotome, N. Kida, S. Horiuchi, and H. Okamoto, Visualization of ferroelectric domains in a hydrogen-bonded molecular crystal using emission of terahertz radiation, Appl. Phys. Lett. **105**, 041101 (2014).

[51] Y. Kinoshita, N. Kida, M. Sotome, R. Takeda, N. Abe, M. Saito, and T. Arima, Visualization of ferroelectric domains in boracite using emission of terahertz radiation, Jpn. J. Appl. Phys. **53**, 09PD08 (2014).

[52] M. Sotome, N. Kida, Y. Kinoshita, H. Yamakawa, T. Miyamoto, H. Mori, and H. Okamoto, Visualization of a nonlinear conducting path in an organic molecular ferroelectric by using emission of terahertz radiation, Phys. Rev. B **95**, 241102(R) (2017).

[53] M. Sotome, N. Kida, S. Horiuchi, and H. Okamoto, Terahertz radiation imaging of ferroelectric domain topography in room-temperature hydrogen-bonded supramolecular ferroelectrics, ACS Photonics **2**, 1373 (2015).

[54] H. Hirori, A. Doi, F. Blanchard, and K. Tanaka, Single-cycle terahertz pulses with amplitudes exceeding 1 MV/cm generated by optical rectification in $LiNbO_3$, Appl. Phys. Lett. **98**, 091106 (2011).

[55] H. Yada, T. Miyamoto, and H. Okamoto, Terahertz-field-driven sub-picosecond optical switching in a one-dimensional Mott insulator enabled by large third-order optical nonlinearity, Appl. Phys. Lett. **102**, 091104 (2013).

[56] T. Yamaguchi, K. Asada, H. Yamakawa, T. Miyamoto, K. Iwano, T. Nakamura, N. Kida, and H. Okamoto, Photoexcitation of a one-dimensional polarization-inverted domain from the charge-ordered ferroelectric ground state of (TMTTF)$_2$PF$_6$, Phys. Rev. B. **99**, 245104 (2019).

[57] M. Dumm, M. Abaker, M. Dressel, and L. K. Montgomery, Charge order in (TMTTF)$_2$PF$_6$ investigated by infrared spectroscopy. J. Low Temp. Phys. **142**, 609 (2006).

[58] J. Favand and F. Mila, Theory of the optical conductivity of (TMTSF)$_2$PF$_6$ in the midinfrared range, Phys. Rev. B **54**, 10425 (1996).

[59] Y. Naitoh, Y. Kawakami, T. Ishikawa, Y. Sagae, H. Itoh, K. Yamamoto, T. Sasaki, M. Dressel, S. Ishihara, Y. Tanaka, K. Yonemitsu, and S. Iwai, Ultrafast response of plasmalike reflectivity edge in (TMTTF)$_2$AsF$_6$ (TMTTF)$_2$AsF$_6$ driven by a 7-fs 1.5-cycle strong-light field, Phys. Rev. B **93**, 165126 (2016).

[60] R. Bozio, M. Meneghetti, and C. Pecile, Optical properties of molecular conductors: One-dimensional systems with twofold-commensurate charge density waves, Phys. Rev. B **36**, 7795 (1987).

[61] U. Fano, Effects of configuration interaction on intensities and phase shifts, Phys. Rev. **124**, 1866 (1961).

[62] D. M. Riffe, Classical Fano oscillator, Phys. Rev. B **84**, 064308 (2011).

[63] M. F. Limonov, M. V. Rybin, A. N. Poddubny, and Y. S. Kivshar, Fano resonances in photonics, Nat. Photonics **11**, 543 (2017).

[64] Y. S. Joe, A. M. Satanin, and C. S. Kim, Classical analogy of Fano resonances, Phys. Scr. **74**, 259 (2006).

[65] A. Painelli and A. Girlando, Electron-molecular vibration (e-mv) coupling in charge-transfer compounds and its consequences on the optical spectra: A theoretical framework, J. Chem. Phys. **84**, 5655 (1986).

[66] D. Pedron, R. Bozio, M. Meneghetti, and C. Pecile, Electron-phonon coupling in low dimensional organic superconductors, Mol. Cryst. Liq. Cryst. **234**, 161 (1993).

[67] D. Faltermeier, J. Barz, M. Dumm, M. Dressel, N. Drichko, B. Petrov, V. Semkin, R. Vlasova, C. Meźière, and P. Batai, Bandwidth-controlled Mott transition in κ-(BEDT-TTF)$_2$Cu[N(CN)$_2$]Br$_x$Cl$_{1-x}$: Optical studies of localized charge excitations, Phys. Rev. B. **76**, 165113 (2007).

[68] P. N. Butcher and D. Cotter, *The Elements of Nonlinear Optics* (Cambridge University Press, Cambridge, 1990).

[69] M. de Souza, P. Foury-Leylekian, A. Moradpour, J.-P. Pouget, and M. Lang, Evidence for Lattice Effects at the Charge-Ordering Transition in (TMTTF)$_2$X, Phys. Rev. Lett. **101**, 216403 (2008).